Assessment of the Free Shear Boundary Condition in a Capillary Meniscus via Molecular Dynamics

Abdul Aziz Shuvo[1], C. Ulises Gonzalez-Valle[2], Xiang Yang[1], Bladimir Ramos-Alvarado[1]

[1]*Department of Mechanical Engineering, The Pennsylvania State University, University Park, PA 16802, USA.*

[2] *Richard J. Resch School of Engineering, University of Wisconsin-Green Bay, Green Bay, WI 54311, USA*

Authors to whom correspondence should be addressed: bzr52@psu.edu and xzy48@psu.edu

Abstract:

Computational fluid dynamics models often employ the free shear boundary condition at free surfaces, a result from the continuity of the stress and the large viscosity contrast at liquid-gas interfaces. This study leverages non-equilibrium molecular dynamics simulations to investigate the validity of the free shear boundary condition on the exposed surface of a liquid meniscus at the nanoscale, provide the first molecular level description of the water-air interface. The primary objective is elucidating the fundamental mechanisms and behaviors of fluid interactions within a capillary meniscus formed between two carbon nanotubes (CNTs) in shear-driven flow. Shear-induced flow simulations were conducted by varying the velocity of a solid slab to induce different shear rates in the adjacent water molecules. The results demonstrate, for the first time, negligible shear at the free surface, supporting the free shear assumption at the nanoscale. A force balance analysis reveals that capillary and surface tension forces dominate within the meniscus, dictating its shape and stability. Meniscus deformation was observed and primarily attributed to interatomic interactions between water molecules and CNTs, driven by a combination of short-range repulsive forces and van der Waals attractions. The minimal contribution from shear forces suggests that interatomic forces, rather than applied shear stress, are the primary drivers of the meniscus deformation. These findings offer valuable insights into fluid behavior and a sound fundamental analysis of the free shear boundary condition at the nanoscale.

I. INTRODUCTION

The accurate modeling of fluid behavior at the free surface (i.e., liquid-gas interfaces) is a critical aspect of computational fluid dynamics (CFD), particularly in applications involving multiphase flows and surface phenomena.[1–3] Traditional CFD approaches often employ the free shear boundary condition at liquid-gas interfaces:

$$\frac{dU_{||}}{dn} = 0, \tag{1}$$

where $U_{||}$ is the velocity parallel to the interface, and n is the coordinate normal to the free surface. This boundary condition assumes that the tangential velocity of the fluid at the boundary is not influenced by the viscous shear force.[4] The validity of the slip condition in Eq. (1) is based on the continuity of the stress at the interface of an unbounded liquid-gas interface:

$$\rho_l \upsilon_l \frac{dU_{||,l}}{dn} = \rho_g \upsilon_g \frac{dU_{||,g}}{dn}, \tag{2}$$

and the fact that the dynamic viscosity of liquids (l) is significantly larger than that of gases (g), i.e.,

$$\rho_l \upsilon_l \gg \rho_g \upsilon_g . \tag{3}$$

here, ρ denotes density, ν denotes kinematic viscosity, the product of the density and the kinematic viscosity gives the dynamic viscosity, the subscripts l and g denote liquid and gas, respectively. Since the velocity gradient on the air side is finite, Eqs. (2, 3) necessarily leads to $dU_{||,l}/dn \approx 0$, i.e., the no-shear stress boundary condition depicted in Eq. (1). However, the force balance in Eq. (2) is valid only if the interface is unbounded. When the interface is bounded, a meniscus forms, as illustrated in Fig. 1(a). This configuration arises in contexts such as superhydrophobic surfaces,[5] where air pockets are trapped between small-scale surface structures. In this scenario, fluid flow experiences less drag at the air interface, thereby reducing drag forces compared to a flat flow situation. Unlike a free interface, a meniscus can sustain a tangential force. Consider the schematic depicted in Figure 1(b), where the force balance yields

$$\frac{dU_{||,l}}{dn} \approx \frac{\sigma(\cos\theta_1 - \cos\theta_2)}{\rho_l \upsilon_l D}, \tag{4}$$

where σ is the surface tension, $\theta_{1,2}$ are the contact angles at the two walls, and D is the size of the meniscus. Here, we have already neglected the viscous force on the air side, which is small, and the no shear condition no longer applies. Nonetheless, CFD models often neglect the shear stress on the meniscus,[6,7] a simplification that lacks a fundamental molecular-level justification.

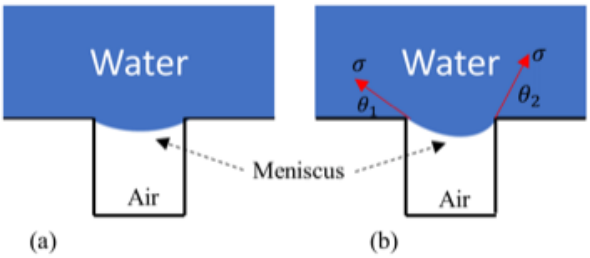

Figure 1. (a) Schematic of a meniscus in equilibrium suspended over a gap, and (b) schematic of the same meniscus but distorted under the effect of shear.

The schematics in Figure 1 resemble the gas-filled gaps observed in microstructured hydrophobic surfaces (Cassie textures), which can be found in nature[8,9] and mimicked through microfabrication.[10] The hydrophobic nature of these patterned surfaces arises from the intermittent weak gas-liquid contact that adds or counteracts any magnitude of the solid-liquid adhesion. Consequently, Cassie textures are known for creating large hydrodynamic slip (approximating free shear) surfaces.[11] However, there is still a lack of consensus on the fundamental understanding of the effective slip (alternating solid- and gas-liquid interfaces), primarily due to the local shear at the free surface.[11–13] Efforts by de Gennes[13] showed that slip at the gas-liquid interface is proportional to the product of the gas gap depth (t) and the liquid/gas viscosity contrast (μ_l/μ_g). For an air-water interface, the gas-liquid slip would be ~50t, which is equivalent to having a free surface boundary condition even for a gap as small as 1 nm. Hendy and Lund[12] used the de Gennes expression to build an analytical model of alternating solid-liquid and free surfaces, where the gas-liquid boundary condition was parametrically assumed. More recently, Nizcaya et al.[11] expanded upon the simplification of the gas cushion model (de Gennes expression) and developed a closed-form solution for predicting slip over patterned surfaces, where again, the gas-liquid interface boundary condition was assumed and never investigated at a fundamental level.

The primary goal of this contribution is to provide fundamental insight into the shear effect on the free surface of a nanoscale hydrophobic capillary meniscus. This work aims to elucidate the mechanisms and

fluid interactions within a water capillary meniscus adjacent to shear-driven flow. To achieve this, we conducted non-equilibrium molecular dynamics (NEMD) simulations of shear-driven flow where a hydrophobic water meniscus acted as a free surface. NEMD directly solves the motions of the molecules in the system. The equation solved is F = ma, where m is the mass of any given molecule in the MD calculation, a is the acceleration, and F is the force experienced by the molecule. This provides more fundamental than a continuum level description offered by the Navier-Stokes equation as used in Oron et al.[14], allowing us to directly test the validity of Eq. (1) for bounded liquid-gas interface. We confirmed that the free-shear boundary condition is a good approximation in nanoscale water menisci given (1) the observed force balance at the solid-gas-liquid interface formed by the meniscus, and (2) the relative magnitude of the observed shear force at the liquid-gas interface.

II. METHODS

The LAMMPS code[15] was used to carry out the NEMD simulations and OVITO[16] for visualization. The computational domain, illustrated in Figure 2, consisted of a water film containing 13,998 molecules having a bulk density of 1.00±0.02 g/cm^3. The simulation box was periodic in the *x*- and *z*-direction, while the *y*-direction, normal to the flow, was fixed. Two carbon nanotubes (CNTs) were immersed in the water film, forming a capillary meniscus between them. The top and bottom confining slabs were diamond-structured carbon. The bottom slab induced shear to the water molecules by applying a tangential velocity (x-direction in Figure 2), see Video1 and Video2 as multimedia available online. Consequently, the large shear velocities generate significant heating, requiring a medium to dissipate thermal energy from the system. In our simulations, a Langevin thermostat was applied to the water atoms in the y- and z-directions to remove the excess heat; thus, creating thermal sinks at 300 K in the flow orthogonal directions, while the flow direction remained unaffected. The top slab remained fixed to maintain the simulation box size.

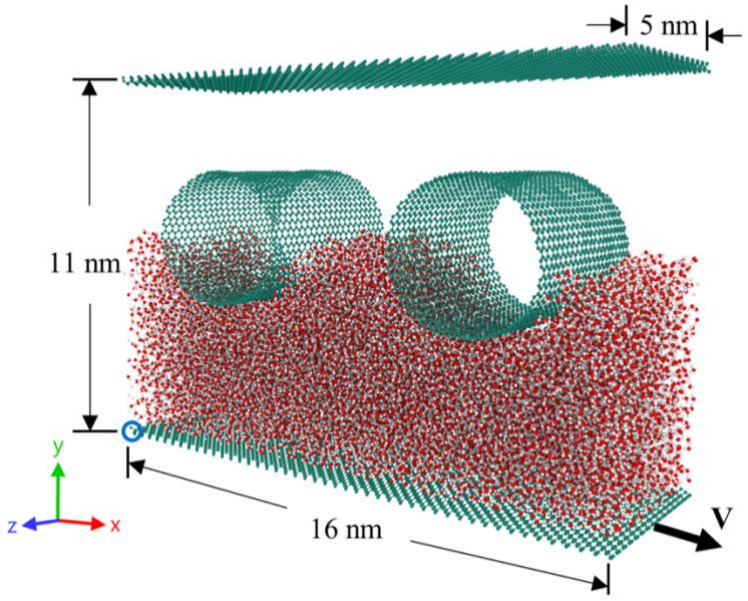

Figure 2. Computational model of the hydrophobic water meniscus. The red spheres represent oxygen atoms, the white spheres represent hydrogen atoms, and the teal spheres represent carbon atoms. The coordinate of the blue circle in the left bottom corner is (0, 1, 5) nm. Multimedia available online as Video1 and Video2.

The SPC/E[17,18] water model was utilized for the water particles and the SHAKE[19] algorithm was implemented to ensure bond rigidity. The cutoff for the pairwise interactions was set to 15 Å, while the long-range Coulombic interactions were computed using the PPPM[20] algorithm with a precision of 1×10^{-6}. The carbon atoms in each CNT were modeled using a Tersoff[21] force field (FF). The solid-liquid interactions were calculated using a 12-6 Lennard-Jones (LJ) FF, and the LJ parameters for the CNT-water interface were derived using the wettability-E_{min} relationship proposed by Ramos-Alvarado[22]. This relationship uses LJ parameters as input and outputs a size-independent contact angle. The LJ parameters for the CNTs-water interactions were ϵ_{CO}= 0.05258 kJ/mol, σ_{CO}=3.19 Å, and ϵ_{CH}=0, σ_{CH}=0. Since we are interested in generating a hydrophobic meniscus, the LJ parameters were chosen such that a contact angle of 136º was observed. Since momentum transfer from the diamond slab to the water depends on solid-liquid affinity and liquid structuring[23], the LJ parameters for the bottom slab-water were greater than the CNT-water ones to ensure effective momentum transfer from the solid to the liquid. The parameters were ϵ_{BO}=1.25ϵ_{CO}, and σ_{BO}=σ_{CO}. Alternatively, the top diamond slab was modeled as a repulsive wall. The simulation approach involved several systematic steps. Initially, all atoms and molecules in the computational box were energy-minimized. Consecutively, and using an NVT ensemble at 300 K, the bottom slab was gradually moved upward to establish a stable meniscus between the CNTs, monitoring the bulk water density. After achieving a stable meniscus, the CNTs and water molecules were equilibrated at 300 K for 1 ns using an NVT ensemble. To confirm stability and equilibration, the system was subsequently run for an additional 5 ns in the microcanonical ensemble (NVE), with continuous monitoring of temperature, pressure, and energy to ensure steadiness. Following equilibration, shear was introduced by moving the bottom slab at a constant velocity. During this stage, which lasted for 2 ns, the water molecules were thermostated as previously indicated to remove viscous heating; the CNTs were fixed in this step. After verifying the stability of temperature, pressure, and energy, the system runs a final 2 ns for data collection. During this period, atomic coordinates, velocities, and forces were recorded at intervals of 500 fs. Four independent sets of simulations were performed to ensure the reliability of the results. The time step for all simulations was set to 1 fs.

III. RESULTS AND DISCUSSION

Figure 3 depicts the density contour $\rho(x,y)$ of water; the density contours were calculated by time-averaging the count of liquid particles per unit volume within bins of dimension 0.32×0.27 Å^2 in the x-y plane during the production run and under shear. The gas-liquid interface region was defined at the locations where $\rho(x,y) = \rho_{bulk}/2$ [24,25], as indicated by the black dots in the contours depicted in the right panels of Figure 3. To characterize the shape of the capillary meniscus, the interface line was fitted with a circular function, as shown in Figure 4(a). The R^2 values for these circular function fits were consistently above 93% for all cases, indicating a high accuracy in this representation of the meniscus shape. It is worth noting that the fluid's shear, $\dot{\gamma}$, was calculated from the resulting linear slope of the velocity profile generated in the water molecules under the meniscus.

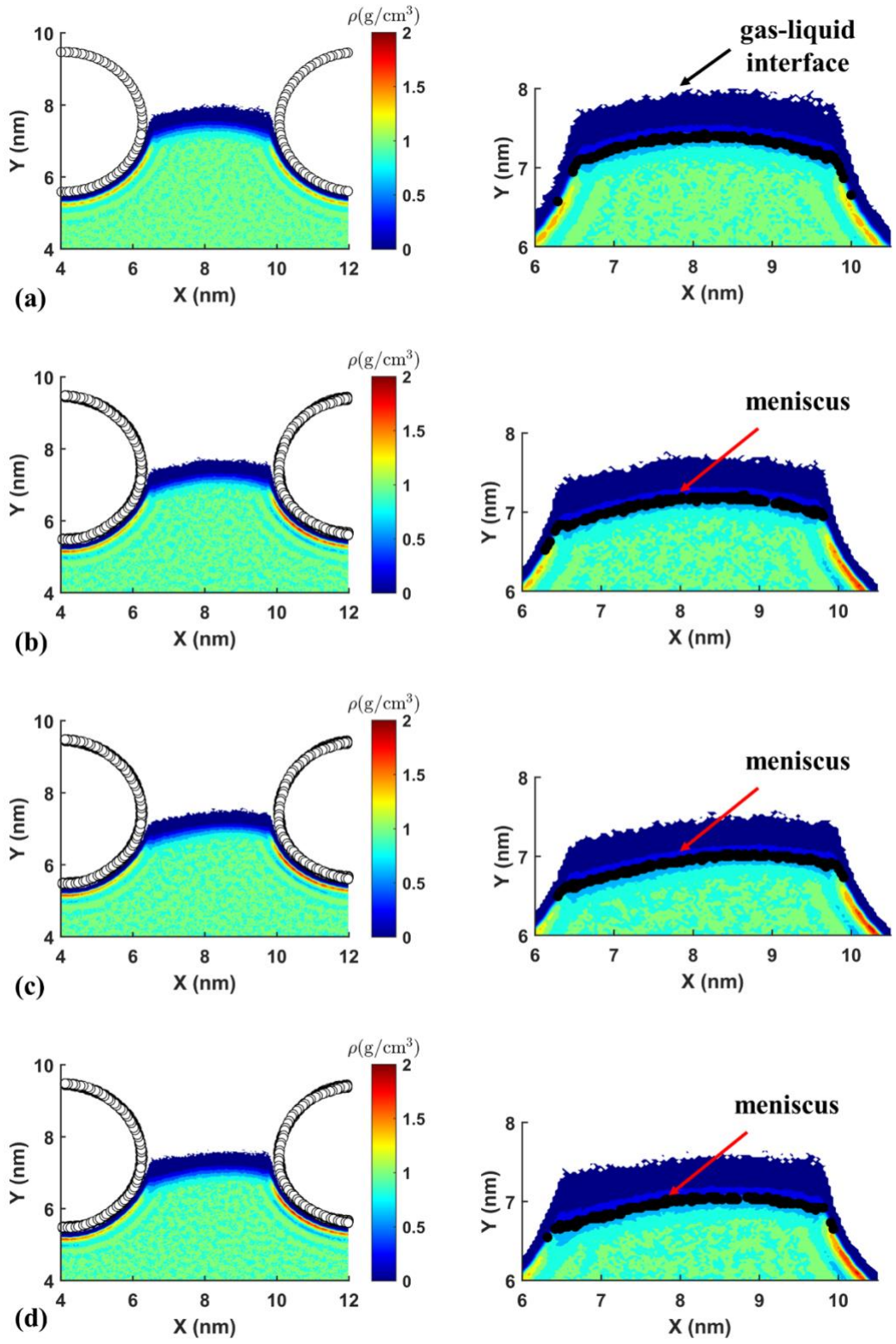

Figure 3. Density contours of water for (a) no-shear, (b) $\dot{\gamma} = 9.8 \times 10^9$ s^{-1} (c) $\dot{\gamma}=12\times10^9$ s^{-1} (d) $\dot{\gamma}=13 \times 10^9$ s^{-1}. The black half rings in the left panel of the figure represent CNTs. The black dots in the right panel represent the interface where $\rho(x,y) = \rho_{bulk}/2$. The shear rate ($\dot{\gamma}$) was obtained from the slope of the fitted velocity profile, as illustrated in Figure 5.

The capillary meniscus deformed under shear, as illustrated in Figure 4(a). This deformation is caused by the complex interplay of repulsive and attractive forces at the molecular level. The movement of water atoms is primarily driven by the applied shear, causing a bias in the way that the water molecules interact with the CNTs. This resulted in an asymmetric deformation of the meniscus under shear, which can be explained by the variation of the parameters of the circular function, $(x-x_c)^2+(y-y_c)^2=r^2$, used to fit the liquid-gas interface. The fitting parameters listed in Table 1 provide quantitative evidence of the meniscus deformation. As the shear rate increases, the values of y_c generally decrease, indicating a lowering of the meniscus height. This trend is consistent with the visual observations in Figure 4(a), where higher shear rates correspond to a flattened meniscus. Additionally, the radius of curvature r tends to increase with higher shear rates, suggesting that the meniscus flattens. The shift in x_c and y_c demonstrates that the centroid of the meniscus moves from left to right (shear direction) with increasing shear rates. This change results in different slope angles at the edges, further confirming the influence of shear on the meniscus shape.

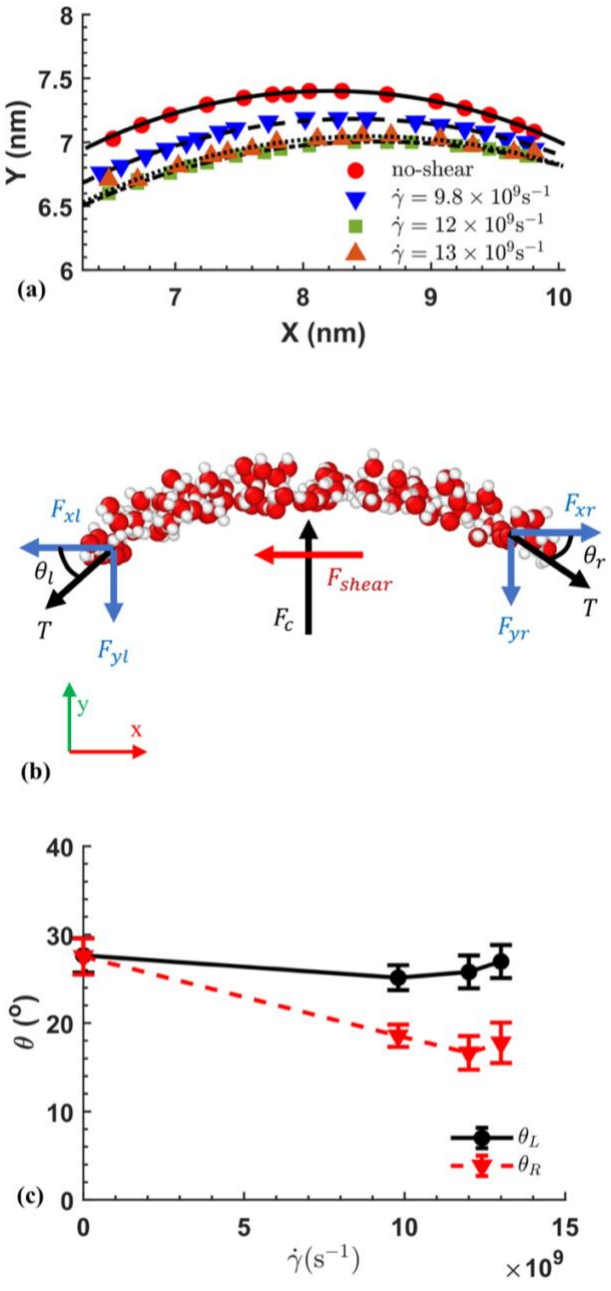

Figure 4. (a) The fitted capillary menisci for all shear rates from the density contour where $\rho(x,y) = \rho_{bulk}/2$. (b) Free body diagram of the meniscus, see Video3 (multimedia available online) for a visualization of water molecules within the control volume. (c)Variation of slope angles on both sides of the capillary meniscus with shear rates.

Table 1. Fitting parameters for the meniscus shape, $(x - x_c)^2 + (y - y_c)^2 = r^2$.

v (m s^{-1})	$\dot{\gamma}$ (s^{-1})	x_c (Å)	y_c (Å)	r (Å)
0	0	81.74±0.19	34.51±3.02	40.66±2.66
300	9.8×10^9	84.24±0.17	20.59±3.54	50.76±3.01
500	12×10^9	85.45±0.40	18.25±4.23	52.47±4.06
700	13×10^9	85.27±0.99	21.02±4.29	49.87±3.83

To further investigate the effect of shear on the capillary meniscus, we analyzed the forces on the meniscus dome. Figure 4(b) illustrates a free-body diagram showing the various forces acting on the meniscus. See Video3 (multimedia available online) for a dynamic visualization of the water molecules forming the meniscus. Figure 4(c) depicts the slope angles (θ_l) and (θ_r) of the meniscus under different $\dot{\gamma}$. It is observed that as the shear rate increases, the slope angle θ_l on the left side remains relatively constant, while θ_r on the right side decreases significantly. This behavior indicates a more pronounced deformation on the right side of the meniscus in the shear-driven flow. The fitting parameters in Table 1 further support these observations, where the centroid of the meniscus shifted towards the right, in the direction of flow, and the radius of curvature r increases, suggesting a spreading of the meniscus. In the free-body diagram, (F_{xl}) and (F_{xr}) represent the lateral forces on the left and right sides of the meniscus, respectively, while (F_{yl}) and (F_{yr}) represent the vertical forces. These forces are the horizontal and vertical components of the surface tension force (T=$\sigma_{SPC/E}L_z$) acting on the meniscus, where $\sigma_{SPC/E}$ and L_z are the surface tension of water and the length of the CNT, respectively. Vo et al.[26] reported $\sigma_{SPC/E}$ = 72.06 mN/m for the SPC/E water model, which we adopted for this study. The capillary force (F_c) was calculated from the capillary pressure (P_c=$\sigma_{SPC/E}\kappa$), where κ is the inverse of the radius of curvature. Table 2 summarizes the lateral force calculations and Table 3 details the normal forces, all normalized by T. The force balance analysis revealed that capillary and surface tension forces dominate near the free surface, while the shear force is comparatively smaller, reaching a maximum of approximately 6% of the surface tension force, as indicated in Table 2. Now, if the meniscus shear force is compared against the shear force in the bulk of the fluid, it represents approximately 2.8%. These calculations agree with the macroscopic view of the free shear boundary condition at the free surfaces. Similarly, the sum of the normal surface tension components matches the capillary force calculated in Table 3, further confirming the adequacy of the formulated force analysis and the circular fit used to represent the meniscus interface.

Table 2. Lateral forces, normalized by the surface tension force (T).

v(ms^{-1})	$\dot{\gamma}\ (s^{-1})$	F_{xl}	F_{xr}	F_{shear}
0	0	-0.89±0.02	0.89±0.02	0
300	9.8×10^9	-0.91 ±0.01	0.95±0.01	-0.04±0.01
500	12×10^9	-0.90±0.01	0.96±0.01	-0.06±0.01
700	13×10^9	-0.89±0.02	0.95±0.01	-0.06±0.01

Table 3. Normal forces normalized by the surface tension force (T).

v(ms^{-1})	$\dot{\gamma}\ (s^{-1})$	F_{yl}	F_{yr}	$F_{yl} + F_{yr}$	F_c
0	0	-0.46±0.03	-0.46±0.03	-0.93±0.06	0.96±0.07
300	9.8×10^9	-0.42±0.02	-0.32±0.02	-0.74±0.04	0.76±0.05
500	12×10^9	-0.43±0.01	-0.29±0.03	-0.72±0.06	0.74±0.06
700	13×10^9	-0.45±0.03	-0.30±0.04	-0.76±0.06	0.78±0.06

For a better visualization of the shear effect near the free surface, we examined the velocity profile in the region below the meniscus. The front view of the computational model in Figure 5 illustrates the domain where the shear velocity was calculated using discrete bins of thickness 3 Å, and the resulting velocity profiles from the bottom (wall imparting a tangential velocity, y = 1 nm) to the edge of the meniscus (6 nm < y < 7 nm). The smallest and largest shear conditions are depicted in Figure 5, and the slopes of the lines used to fit the data represent $\dot{\gamma}$. It is evident from the data that there is no significant shear at the location of the capillary meniscus, illustrated by the yellow-shaded region in the inset of the right-side panel of Figure 5; where the notorious slope of the lines representing the water's velocity profiles transition to steeper profiles (aligned with the y-axis in Figure 5) near the liquid-gas interface. These observations align with the conventional microscopic free shear boundary condition at the free surface and the small calculation of shear forces detailed in Table 2.

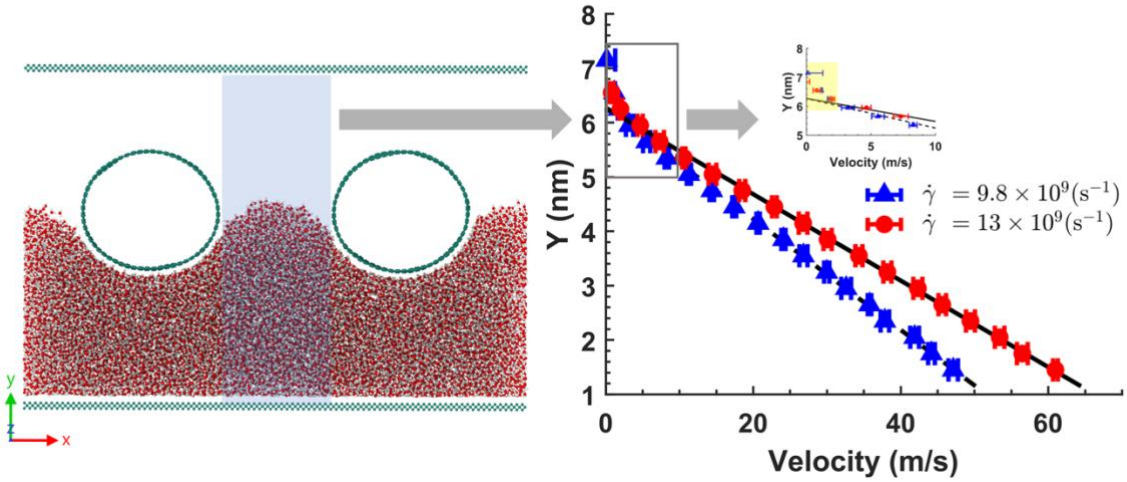

Figure 5. (Left panel) The water velocity profile was calculated within the blue-shaded region. (Right panel) Velocity profiles are calculated for extreme shear rates. The yellow-shaded region in the inset indicates the location of the capillary meniscus. The results demonstrate that there is negligible shear near the free surface, as illustrated by the steep velocity profiles near the meniscus.

CONCLUSIONS

We investigated the effect of shear flow near the free surface of a capillary meniscus using NEMD simulations, providing a molecular level description of the water-air interface for the first time. The force balance analysis indicated that capillary and surface tension forces are the primary determinants of the meniscus shape and stability. The shear force contribution was minimal, reaching a maximum of approximately 2.8% of the shear in the bulk of the fluid. The meniscus interface fitting parameters revealed that as the shear rate increases, the meniscus flattens while its centroid shifts towards the direction of flow. Moreover, the water velocity profiles confirmed that there is no significant shear at the location of the capillary meniscus (liquid-gas interface). These observations are consistent with the traditional free-shear boundary conditions used in computational fluid dynamics and represent the first molecule-level evidence for the no stress condition at the water-air interface.

ACKNOWLEDGMENTS

This research is supported by the National Science Foundation, USA (Award number: 2241730). Yang acknowledges DARPA grant number HR00112490345 with Susan Swithenbank as the technical monitor.

AUTHOR DECLARATIONS

Conflict of Interest

The authors have no conflicts to disclose.

DATA AVAILABILITY

The data that support the findings of this study are available from the corresponding authors upon reasonable request.

REFERENCES

[1] R. Scardovelli, and S. Zaleski, "DIRECT NUMERICAL SIMULATION OF FREE-SURFACE AND INTERFACIAL FLOW," Annu Rev Fluid Mech **31**(1), 567–603 (1999).

[2] C.W. Hirt, and B.D. Nichols, "Volume of fluid (VOF) method for the dynamics of free boundaries," J Comput Phys **39**(1), 201–225 (1981).

[3] R. Verzicco, "Immersed Boundary Methods: Historical Perspective and Future Outlook," Annu Rev Fluid Mech **55**(1), 129–155 (2023).

[4] A. Prosperetti, and G. Tryggvason, *Computational Methods for Multiphase Flow* (Cambridge university press, 2009).

[5] J. Jeevahan, M. Chandrasekaran, G. Britto Joseph, R.B. Durairaj, and G. Mageshwaran, "Superhydrophobic surfaces: a review on fundamentals, applications, and challenges," J Coat Technol Res **15**(2), 231–250 (2018).

[6] M.B. MARTELL, J.B. PEROT, and J.P. ROTHSTEIN, "Direct numerical simulations of turbulent flows over superhydrophobic surfaces," J Fluid Mech **620**, 31–41 (2009).

[7] M.B. Martell, J.P. Rothstein, and J.B. Perot, "An analysis of superhydrophobic turbulent drag reduction mechanisms using direct numerical simulation," Physics of Fluids **22**(6), (2010).

[8] T. Darmanin, and F. Guittard, "Recent advances in the potential applications of bioinspired superhydrophobic materials," J. Mater. Chem. A **2**(39), 16319–16359 (2014).

[9] E.J. Falde, S.T. Yohe, Y.L. Colson, and M.W. Grinstaff, "Superhydrophobic materials for biomedical applications," Biomaterials **104**, 87–103 (2016).

[10] J.T. Simpson, S.R. Hunter, and T. Aytug, "Superhydrophobic materials and coatings: a review," Reports on Progress in Physics **78**(8), 086501 (2015).

[11] T. V. Nizkaya, E.S. Asmolov, and O.I. Vinogradova, "Gas cushion model and hydrodynamic boundary conditions for superhydrophobic textures," Phys Rev E **90**(4), 043017 (2014).

[12] S.C. Hendy, and N.J. Lund, "Effective slip boundary conditions for flows over nanoscale chemical heterogeneities," Phys Rev E **76**(6), 066313 (2007).

[13] P.G. de Gennes, "On Fluid/Wall Slippage," Langmuir **18**(9), 3413–3414 (2002).

[14] A. Oron, S.H. Davis, and S.G. Bankoff, "Long-scale evolution of thin liquid films," Rev Mod Phys **69**(3), 931–980 (1997).

[15] S. Plimpton, "Fast Parallel Algorithms for Short-Range Molecular Dynamics," J Comput Phys **117**(1), 1–19 (1995).

[16] A. Stukowski, "Visualization and analysis of atomistic simulation data with OVITO-the Open Visualization Tool," Model Simul Mat Sci Eng **18**(1), 015012 (2010).

[17] G. Ciccotti, and J.P. Ryckaert, "Molecular dynamics simulation of rigid molecules," Computer Physics Reports **4**, 346–392 (1986).

[18] H.J.C. Berendsen, J.R. Grigera, and T.P. Straatsma, "The missing term in effective pair potentials," J Phys Chem **91**(24), 6269–6271 (1987).

[19] J.-P. Ryckaert, G. Ciccotti, and H.J.C. Berendsen, "Numerical integration of the cartesian equations of motion of a system with constraints: molecular dynamics of n-alkanes," J Comput Phys **23**(3), 327–341 (1977).

[20] R.W. Hockney, and J.W. Eastwood, *Computer Simulation Using Particles* (CRC Press, 1988).

[21] L. Lindsay, and D.A. Broido, "Optimized Tersoff and Brenner empirical potential parameters for lattice dynamics and phonon thermal transport in carbon nanotubes and graphene," Phys Rev B Condens Matter Mater Phys **81**(20), 205441 (2010).

[22] B. Ramos-Alvarado, "Water wettability of graphene and graphite, optimization of solid-liquid interaction force fields, and insights from mean-field modeling," Journal of Chemical Physics **151**(11), 114701 (2019).

[23] A.A. Shuvo, L.E. Paniagua-Guerra, X. Yang, and B. Ramos-Alvarado, "Hydrodynamic slip characteristics of shear-driven water flow in nanoscale carbon slits," J Chem Phys **160**(19), (2024).

[24] B. Ramos-Alvarado, S. Kumar, and G.P. Peterson, "Hydrodynamic slip in silicon nanochannels," Phys Rev E **93**(3), 033117 (2016).

[25] B. Ramos-Alvarado, S. Kumar, and G.P. Peterson, "On the wettability transparency of graphene-coated silicon surfaces," J Chem Phys **144**(1), (2016).

[26] T.Q. Vo, M. Barisik, and B. Kim, "Near-surface viscosity effects on capillary rise of water in nanotubes," Phys Rev E Stat Nonlin Soft Matter Phys **92**(5), (2015).